Non-Reciprocal, Robust Surface Plasmon Polaritons on Gyrotropic Interfaces

Samaneh Pakniyat, *Student Member, IEEE*, Alexander M. Holmes, *Student Member, IEEE*, George W. Hanson, *Fellow, IEEE*, S. Ali Hassani Gangaraj, *Member, IEEE*, Mauro Antezza, Mário G. Silveirinha, *Fellow, IEEE*, Shahrokh Jam, *Senior Member, IEEE*, and Francesco Monticone, *Member, IEEE*

***Abstract*— Unidirectional surface plasmon polaritons (SPPs) at the interface between a gyrotropic medium and a simple medium are studied in a newly recognized frequency regime wherein the SPPs form narrow, beam-like patterns due to quasi-hyperbolic dispersion. The SPP beams are steerable by controlling parameters such as the cyclotron frequency (external magnetic bias) or the frequency of operation. The bulk band structure along different propagation directions is examined to ascertain a common bulk bandgap, valid for all propagation directions, which the SPPs cross. In addition, group velocity and Poynting vector for the SPPs are presented. The case of a finite-thickness gyrotropic slab is also considered, for which we present the Green function and examine the thickness and loss level required to maintain a unidirectional SPP.**

***Index Terms*— Directed surface plasmon polariton (SPP), Green's function, gyrotropic.**

I. Introduction

THE properties of surface plasmon polaritons (SPPs) in different biased plasma configurations have been widely studied [1]–[5]; see the comprehensive review in [6]. Some of these basic configurations are: 1) the external magnetic bias is perpendicular to the interface and, correspondingly, the SPP propagation vector; 2) the magnetic bias is parallel to the interface, but perpendicular to the propagation vector, called the Voigt configuration; and 3) the magnetic bias is parallel to the interface and also parallel to the propagation vector, known as the Faraday configuration. In [7], the well-known Voigt configuration was reexamined, and it was shown that the SPPs have topological properties, making contact with the current work in photonic topological insulators, which, previously, were investigated for periodic media [8], [9].

Nonreciprocal topological surface waves have several important features; namely, they are unidirectional and they operate in the bulk bandgap of a topologically nontrivial material [8]–[10]. Being strongly nonreciprocal, upon encountering a discontinuity, they are immune to backscattering, and because they operate in the bulk bandgap, they do not radiate into the bulk. As such, they are forced to pass over the discontinuity, and the lack of scattering or diffraction makes them interesting from a wave-propagation aspect and promising for device applications [11]–[13]. Topological SPPs can be characterized by an integer invariant (e.g., the Chern number), which cannot change except when the underlying momentum-space topology of the bulk bands is changed [14]–[18]. Thus, another view of the reflection- and diffraction-free aspect of topological SPPs is that they are governed by bulk material properties, so that they are not sensitive to surface features and can only change qualitatively when the bulk topology changes. A change in topology arises when a bandgap is closed or opened, which occurs for the biased plasma when the bias field is reversed in direction.

The continuum plasma case of Voigt topological SPPs identified in [7] was studied in [14], [17], [19], and [20]. SPPs in the Voigt configuration cross the bulk bandgap and therefore exist above the plasma frequency. Recently, it was observed that SPPs exist below the bandgap, propagating at various angles with respect to the bias direction [21], [22]. Those works were focused on the quantum force on a decaying atom, and in [23] the excitation of these modes was considered using circular-polarized dipole sources. In the present work, we investigate these below-the-gap SPPs in more detail. These SPPs are, similar to topological SPPs, unidirectional, operate in a bulk bandgap (and so are diffraction-free), and

Manuscript received February 24, 2019; revised September 25, 2019; accepted October 25, 2019. Date of publication February 3, 2020; date of current version May 5, 2020. The work of Samaneh Pakniyat, Alexander M. Holmes, and George W. Hanson was supported by the National Science Foundation (NSF) under Grant EFMA-1741673. The work of S. Ali Hassani Gangaraj and Francesco Monticone was supported in part by the Air Force Office of Scientific Research under Grant FA9550-19-1-0043 and in part by the National Science Foundation under Grant 1741694. The work of Mário G. Silveirinha was supported by Fundação para Ciência e a Tecnologia (FCT) under Project UIDB/50008/2020. *(Corresponding authors: Alexander M. Holmes; George W. Hanson.)*

Samaneh Pakniyat is with the Department of Electrical Engineering, University of Wisconsin–Milwaukee, Milwaukee, WI 53211 USA, and also with the Department of Electrical and Electronic Engineering, Shiraz University of Technology, Shiraz 13876-71557, Iran (e-mail: pakniyat@uwm.edu).

Alexander M. Holmes and George W. Hanson are with the Department of Electrical Engineering, University of Wisconsin–Milwaukee, Milwaukee, WI 53211 USA (e-mail: holmesam@uwm.edu; george@uwm.edu).

S. Ali Hassani Gangaraj and Francesco Monticone are with the School of Electrical and Computer Engineering, Cornell University, Ithaca, NY 14853 USA (e-mail: ali.gangaraj@gmail.com; francesco.monticone@cornell.edu).

Mauro Antezza is with the Laboratoire Charles Coulomb (L2C), UMR 5221 CNRS-Université de Montpellier, F-34095 Montpellier, France (e-mail: mauro.antezza@umontpellier.fr).

Mário G. Silveirinha is with the Instituto Superior Técnico, University of Lisbon, 1049-001 Lisbon, Portugal, and also with the Instituto de Telecomunicações, University of Lisbon, 1049-001 Lisbon, Portugal (e-mail: mario.silveirinha@co.it.pt).

Shahrokh Jam is with the Department of Electrical and Electronic Engineering, Shiraz University of Technology, Shiraz 13876-71557, Iran (e-mail: jam@sutech.ac.ir).

Color versions of one or more of the figures in this article are available online at http://ieeexplore.ieee.org.

Digital Object Identifier 10.1109/TAP.2020.2969725

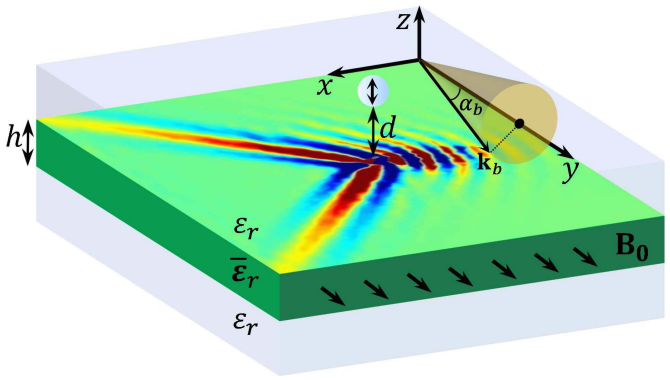

Fig. 1. Slab of gyrotropic material with finite thickness h. The slab is biased with a static magnetic field along the y-axis. A vertical dipole is suspended a distance d above the slab and is responsible for exciting the displayed field pattern near the top surface of the slab. The wavenumber associated with a bulk mode propagating within the slab is denoted as $\mathbf{k}_b$ and is represented in a local coordinate system where α_b denotes the angle that $\mathbf{k}_b$ makes with respect to the y-axis. In the following, ρ refers to the radial distance in the $x-y$ plane.

only change their properties qualitatively when the topology of momentum space is changed. Moreover, and unlike the previously studied topological SPPs, they form narrow beam-like patterns, similar to the case of hyperbolic media [24], [25]. However, it seems difficult or perhaps impossible to assign a topological integer invariant to describe these SPPs as they propagate in different directions at different frequencies within the gap, and so, strictly speaking, these SPPs are not topological. Nevertheless, we show that they still exhibit unidirectional propagation and inherent robustness to discontinuities.

In the following, we have identified a bulk bandgap common to all propagation directions of the plasma bulk modes, within which the SPPs exist. This common bandgap is discussed, the behavior of the SPPs in different frequency regimes is determined, power flow, group velocity, and Poynting vector are dicussed, and a Green function is obtained for a finite-thickness gyrotropic layer. Additionally, we investigate the backscattering immune properties of a surface wave propagating at the magnetized plasma–air interface and also on the surface of a magnetized plasma slab in the presence of a defect in the lower bandgap frequency regime.

II. Bulk-Mode and SPP Dispersion Analysis

The geometry of interest is depicted in Fig. 1, showing a finite-thickness gyrotropic slab of thickness h, immersed in a simple medium characterized by ε_r. The gyrotropic medium is assumed to be a plasma biased by a static external magnetic field $\mathbf{B}_0 = \hat{\mathbf{y}}B_0$. Assuming time harmonic variation $e^{-i\omega t}$, the magnetized plasma is characterized by the dielectric tensor,

$$\bar{\varepsilon}_r = \varepsilon_t(\bar{\mathbf{I}} - \hat{\mathbf{y}}\hat{\mathbf{y}}) + i\varepsilon_g(\hat{\mathbf{y}} \times \bar{\mathbf{I}}) + \varepsilon_a\hat{\mathbf{y}}\hat{\mathbf{y}} \tag{1}$$

where the permittivity elements, $\{\varepsilon_t, \varepsilon_a, \varepsilon_g\}$ are [26]

$$\varepsilon_t = 1 - \frac{\omega_p^2(1 + i\Gamma/\omega)}{(\omega + i\Gamma)^2 - \omega_c^2}$$
$$\varepsilon_a = 1 - \frac{\omega_p^2}{\omega(\omega + i\Gamma)}, \quad \varepsilon_g = \frac{\omega_c\omega_p^2}{\omega[\omega_c^2 - (\omega + i\Gamma)^2]} \tag{2}$$

such that $\omega_p = \sqrt{Nq_e^2/m^*\varepsilon_0}$, $\omega_c = -q_eB_0/m^*$, and $\Gamma = 1/\tau$ denote the plasma, cyclotron, and collision frequencies, respectively, where N is the free electron density, $q_e = -e$ is the electron charge, m^* is the effective electron mass, and τ is the relaxation time between collisions. This permittivity model is representative of a common gas plasma and is a simplified model of solid state plasma like InSb [26]. It is also a local model; as studied in [27] and [28], a nonlocal model leads to the presence of a backward propagating modes. However, the effect of nonlocality is evident only for very large wavenumbers, and the backward waves vanish when considering realistic levels of loss [23], [28], and so nonlocality is ignored here. Throughout this article, unless otherwise noted, we use the following values for the magnetized plasma: $\omega_p = 2\pi(20\ \text{THz})$, $\Gamma = 0.015\omega_p$, and $\omega_c/\omega_p = 0.4$. The cyclotron frequency is associated with $B_0 = 6.3$ T using the effective mass $m^* = 0.022\text{m}_\text{e}$, where m_e is the electron mass [26].

A. Dispersion of Bulk Modes in a Gyrotropic Medium—the Existence of a Common Bandgap

The characteristics of the bulk modes in an anisotropic medium depend on the direction of propagation. In a structure exhibiting bulk bandgaps, these gaps will also be direction dependent. In this section, we study the bulk dispersion behavior of a gyrotropic medium in order to identify a bulk bandgap, common to all propagation directions. We begin with a plane wave having wavevector $\mathbf{k}_b$, propagating in a gyrotropic medium at angle α_b, with respect to the bias field (the y-direction). Assuming a plane wave solution to Maxwell's equations leads to a homogeneous system of equations for which non-trivial solutions are obtained when [29]–[33]

$$\left|k_0^2\bar{\varepsilon}_r - k_b^2\bar{\mathbf{I}} + \mathbf{k}_b\mathbf{k}_b\right| = 0 \tag{3}$$

where k_0 is the free space wavenumber. Considering $\mathbf{k}_b = \mathbf{k}_t + \hat{\mathbf{y}}k_y$ such that $|\mathbf{k}_t| = k_b \sin\alpha_b$ and $k_y = k_b\cos\alpha_b$, the evaluation of the determinant leads to the dispersion equation for the bulk modes

$$0 = \left[\left(\varepsilon_t^2 - \varepsilon_g^2 + \varepsilon_a\varepsilon_t\right)\sin^2\alpha_b + 2\varepsilon_a\varepsilon_t\cos^2\alpha_b\right]k_0^2k_b^2 - (\varepsilon_t\sin^2\alpha_b + \varepsilon_a\cos^2\alpha_b)k_b^4 - \varepsilon_a\left(\varepsilon_t^2 - \varepsilon_g^2\right)k_0^4. \tag{4}$$

The dispersion diagrams associated with the bulk modes of the biased plasma with different propagation angles are shown in Fig. 2. Fig. 2(a) and (b) show the dispersion of bulk modes which propagate parallel ($\alpha_b = 0°$) and perpendicular ($\alpha_b = 90°$) to the magnetic bias, respectively. In the perpendicular case, the plane wave can be decoupled into a TE (with electric field along the magnetic bias) and a TM (with electric field in a plane perpendicular to the bias direction) wave. They are known as the ordinary and the extraordinary waves, respectively. In the parallel case, the plane wave can be decoupled into left- and right-handed circularly polarized waves [29], [30]. Otherwise, the waves have a hybrid nature.

The two intersection points in the parallel case correspond to Weyl points that arise from crossings between longitudinal plasma modes and transverse helical modes [34]. Fig. 2(c) and (d) show the dispersion for two arbitrary angles in the range, $0° < \alpha_b < 90°$. As seen in Fig. 2, there are four dispersion branches. The second branch from the top (red dashed line) corresponds to a wave which is independent of the magnetic bias and does not lead to a topological SPP (it is the

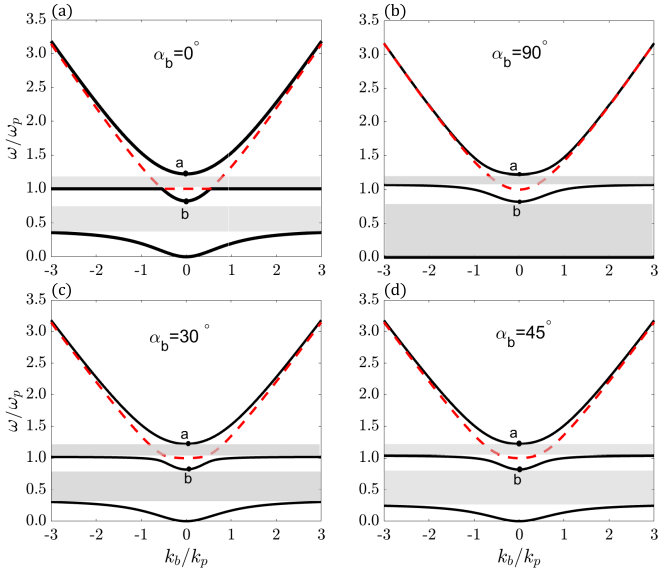

Fig. 2. Dispersion diagram of biased plasma bulk modes for different angles of propagation, where $k_p = \omega_p/c$. Gray-shaded regions highlight bandgaps in the dispersion. The red dashed line corresponds to a wave which is independent of bias, while the black solid lines correspond to the waves which are dependent on bias.

TE wave in the perpendicular case, $\alpha_b = 90°$). Although the flat dashed red section in Fig. 2(a) may appear to naturally belong to the flat black solid dispersion line, the situation admits two viewpoints. For $\alpha_b = 0$ in the lossless case, one could view the horizontal black line as continuing through the red dashed section, since this represents one polarization, whereas the parabolic sections represent a different polarization. That is, there is an eigenvalue degeneracy but not an eigenfunction degeneracy. However, analytic continuation for small nonzero angles indicates that the parabolic red dashed section continues to the nearly flat red dashed section (this is evident in Fig. 2(c) but is more prominent for smaller angles). The eigenfunctions (and in this case also the eigenvalues) cannot be globally defined as smooth analytical functions in k-space.

Two bandgaps form between the other three branches as shown in the shaded regions of Fig. 2. The size of the bandgaps depend on the propagation direction as well as the magnetic bias field strength. The upper bandgap is smallest when $\alpha_b = 90°$. Conversely, the lower bandgap is smallest when $\alpha_b = 0°$. As such, we take the smallest upper (lower) bandgap to represent the upper (lower) bandgap common for all propagation angles, $0° < \alpha_b < 90°$. Points a and b do not change with the propagation angle. The common bandgap and its impact on surface waves is considered further in the following.

B. SPP Dispersion

A surface wave that propagates along the interface between a gyrotropic medium and an isotropic medium, with propagation angle ϕ_s with respect to the x-axis, has wavevector $\mathbf{k}_s = \hat{\mathbf{x}}k_x + \hat{\mathbf{y}}k_y$ in the xoy plane. From the bulk dispersion equation describing the biased plasma (4), we obtain the solutions $\hat{\mathbf{k}}^{\pm}_{b,j} = \mathbf{k}_s \pm \hat{\mathbf{z}}i\gamma_j$ for $j \in \{1, 2\}$, where

$$\gamma_1 = \sqrt{k_x^2 + \frac{1}{2}\left(\kappa - \sqrt{\kappa^2 - \upsilon}\right)} \tag{5}$$

$$\gamma_2 = \sqrt{k_x^2 + \frac{1}{2}\left(\kappa + \sqrt{\kappa^2 - \upsilon}\right)} \tag{6}$$

such that

$$\kappa = \left\{(\varepsilon_t + \varepsilon_a)k_y^2 - \left[\varepsilon_t(\varepsilon_t + \varepsilon_a) - \varepsilon_g^2\right]k_0^2\right\}/\varepsilon_t \tag{7}$$

$$\upsilon = \left\{4\varepsilon_a\left[(\varepsilon_t + \varepsilon_g)k_0^2 - k_y^2\right]\left[(\varepsilon_t - \varepsilon_g)k_0^2 - k_y^2\right]\right\}/\varepsilon_t \tag{8}$$

and in the isotropic dielectric regions, the solutions are simply $\hat{\mathbf{k}}^{\pm} = \mathbf{k}_s \pm \hat{\mathbf{z}}i\gamma_0$ where $\gamma_0 = \sqrt{k_s^2 - k_0^2\varepsilon_r}$. The dispersion relation for the SPP can be obtained by matching the tangential components of the electric and magnetic fields at the interface [21], leading to the 4×4 system of homogeneous equations,

$$\begin{pmatrix} \beta_1^- & \beta_2^- & k_y & i\gamma_0 k_x \\ k_y\theta_1 & k_y\theta_2 & -k_x & i\gamma_0 k_y \\ k_y\phi_1^- & k_y\phi_2^- & i\gamma_0 k_x & -k_0^2\varepsilon_r k_y \\ -\delta_1 k_{t,1}^2 & -\delta_2 k_{t,2}^2 & i\gamma_0 k_y & k_0^2\varepsilon_r k_x \end{pmatrix} \begin{pmatrix} A_1 \\ A_2 \\ B_1 \\ B_2 \end{pmatrix} = \mathbf{0} \tag{9}$$

where $\beta_j^{\pm}$, $\phi_j^{\pm}$, δ_j, and θ_j ($j \in \{1, 2\}$) are defined in the appendix [see (91)]. Nontrivial solutions are obtained when the determinant of the coefficient matrix on the left-hand side of (9) is set equal to zero. Evaluation of the determinant and dividing through by a factor of $-ik_s^2 k_y/\varpi_1\varpi_2\xi_1\xi_2 \neq 0$, where ϖ_j and ξ_j ($j \in \{1, 2\}$) are defined in the appendix [see (91)], leading to the SPP dispersion equation

$$0 = \left(k_y^2 - \gamma_0^2\right)Q_A - k_x Q_B^- + k_x k_y^2 Q_C^- - \left(k_x^2 - \gamma_0^2\right)Q_D^- + \gamma_0(Q_E^- - \varepsilon_r\chi^-) \tag{10}$$

where the quantities Q_A, Q_B^-, Q_C^-, Q_D^-, Q_E^-, and χ^- are defined in the appendix [see (83)–(87) and (90)].

For the well-studied case of propagation perpendicular to the bias ($k_y = 0$), the SPP dispersion is found to be [6], [7]

$$\sqrt{k_x^2 - k_0^2} + \frac{\sqrt{k_x^2 - k_0^2\varepsilon_{eff}}}{\varepsilon_{eff}} = \frac{\varepsilon_g k_x}{\varepsilon_t\varepsilon_{eff}} \tag{11}$$

where $\varepsilon_{eff} = (\varepsilon_t^2 - \varepsilon_g^2)/\varepsilon_t$. However, for $k_y \neq 0$, the general dispersion equation (10) must be used.

III. Green Function for a Finite-Thickness Plasma

In the last section, we considered a simple material-gyrotropic plasma interface, the Green function for which is provided in [21]. In this section, we expand that analysis to consider a finite-thickness gyrotropic layer. We present a closed-form expression (as a Sommerfeld integral) for the Green function in the simple dielectric regions above and below the slab. Importantly, we also provide the Green function coefficient in quotient form for each case, which leads to the identification of the SPP dispersion equation (setting the denominator to zero).

The procedure to derive the Green function follows that in [21] and [35]. The incident field excited by an electric dipole source, with dipole moment $\mathbf{p} = \hat{\mathbf{x}}p_x + \hat{\mathbf{y}}p_y + \hat{\mathbf{z}}p_z$ suspended a

distance d above the first interface, is given by $\mathbf{E}^p(\mathbf{r}) = (\nabla\nabla + \bar{\mathbf{I}}k_0^2\varepsilon_r) \cdot \pi^p(\mathbf{r})$, where $\pi^p(\mathbf{r})$ denotes the principal Hertzian potential due to the dipole source, which we write in terms of the principal Green function, $\pi^p(\mathbf{r}) = g^p(\mathbf{r}, \mathbf{r}_0)\mathbf{p}/\varepsilon_0\varepsilon_r$, where $g^p(\mathbf{r}, \mathbf{r}_0) = e^{ik_0\sqrt{\varepsilon_r}|\mathbf{r}-\mathbf{r}_0|}/4\pi|\mathbf{r}-\mathbf{r}_0|$ such that ε_r is the relative permitivitty of the top and bottom media (see Fig. 1) and $\mathbf{r}_0$ denotes the source point location. Following [21], the reflected and transmitted electric fields for a biased-plasma slab of finite thickness are written as Sommerfeld integrals

$$\mathbf{E}^r(\mathbf{r}) = \int d^2\mathbf{k}_s e^{i\mathbf{k}_s\cdot(\mathbf{r}-\mathbf{r}_0)} \frac{e^{-\gamma_0(d+z)}}{8\pi^2\varepsilon_0\varepsilon_r\gamma_0} \bar{\mathbf{C}}^r \cdot \mathbf{p} \tag{12}$$

$$\mathbf{E}^t(\mathbf{r}) = \int d^2\mathbf{k}_s e^{i\mathbf{k}_s\cdot(\mathbf{r}-\mathbf{r}_0)} \frac{e^{-\gamma_0(d-z)}}{8\pi^2\varepsilon_0\varepsilon_r\gamma_0} \bar{\mathbf{C}}^t \cdot \mathbf{p} \tag{13}$$

where $\bar{\mathbf{C}}^r$ and $\bar{\mathbf{C}}^t$ are tensors defined in the appendix which are written in terms of the reflection and transmission matrices for the biased-plasma slab. Taking into account that the scattered magnetic field is $\mathbf{H}(\mathbf{k}_s, z) = \mathbf{k}_0 \times \mathbf{E}(\mathbf{k}_s, z)/\omega\mu_0$, the Poynting vector can be obtained using $\langle\mathbf{S}\rangle = \mathrm{Re}(\mathbf{E} \times \mathbf{H}^*)/2$.

In all of the numerical examples to follow, we consider the z component of the scattered electric field due to a z directed dipole moment, $\mathbf{p} = \hat{\mathbf{z}}p_z$, placed at a height d above a symmetric slab of thickness h for which $\varepsilon_r = 1$ and $\mathbf{r}_0 = (0, 0, d)$. In this case, the z component of the scattered field simplifies to

$$E_z^r(\mathbf{r}) = \int d^2\mathbf{k}_s e^{i\mathbf{k}_s\cdot\mathbf{r}} \frac{e^{-\gamma_0(d+z)}}{8\pi^2\varepsilon_0\gamma_0} C_{zz}^r p_z \tag{14}$$

$$E_z^t(\mathbf{r}) = \int d^2\mathbf{k}_s e^{i\mathbf{k}_s\cdot\mathbf{r}} \frac{e^{-\gamma_0(d-z)}}{8\pi^2\varepsilon_0\gamma_0} C_{zz}^t p_z. \tag{15}$$

IV. Quasi-Static Approximation

Further insight into the SPPs excited on the surfaces of the magnetized-plasma slab can be gained by a quasi-static approximation, where the electric field is written in terms of the electrostatic potential, ϕ_k, such that $E_k \approx -\nabla\phi_k$, assuming the associated magnetic field is negligible. Solving Gauss' law in both isotropic and gyrotropic media, and applying boundary conditions for the tangential components of the electric field at each interface, the electric potential for a slab shown in Fig. 1 is obtained as $\phi_k = CF(z)e^{i\mathbf{k}_s\cdot\mathbf{r}}$, where C is an amplitude constant and

$$F = \begin{cases} e^{-k_s z}, & z > 0 \\ \cosh\tilde{k}_s z + i\alpha\sinh\tilde{k}_s z, & -h < z < 0 \\ (\cosh\tilde{k}_s h - i\alpha\sinh\tilde{k}_s h)e^{k_s(z+h)}, & z < -h \end{cases} \tag{16}$$

such that $k_s = \sqrt{k_x^2 + k_y^2}$, $\tilde{k}_s = \sqrt{k_x^2 + \varepsilon_a k_y^2/\varepsilon_t}$, and α is a complicated function of material parameters and wavenumbers (omitted since it is not needed in the following). Enforcing continuity of the normal components of electric displacement at the two interfaces leads to the quasi-static SPP dispersion relation

$$\varepsilon_g^2 k_x^2 - \varepsilon_t^2\tilde{k}_s^2 - \varepsilon_r^2 k_s^2 = 2\varepsilon_r\varepsilon_t k_s\tilde{k}_s\coth\tilde{k}_s h. \tag{17}$$

The quasi-static approximation is valid only for SPPs with short wavelength ($k_s \to \infty$). In the limit $h \to \infty$, the dispersion relation reduces to that derived for a single interface [21]

$$\varepsilon_r k_s + k_x\varepsilon_g + \tilde{k}_s\varepsilon_t = 0. \tag{18}$$

By substituting the dispersive model (2), $k_x = k_s\cos\phi_s$ and $k_y = k_s\sin\phi_s$ into (18), where k_s and ϕ_s are the SPP wavenumber and the propagation angle with respect to x-axis, the solutions $\omega_{\mathbf{k}}$ can be found as [21]

$$\omega_{\mathbf{k_s}} = \frac{1}{2}\omega_c\cos\phi_s + \frac{1}{2}\sqrt{2\omega_p^2 + \omega_c^2(1 + \sin^2\phi_s)}. \tag{19}$$

They represent the SPP modes with short wavelength which are only dependent on the SPPs directions, ϕ_s.

V. Results

As considered in recent photonic topological work, we are interested in bulk bandgap crossing SPPs. Since the upper bandgap for the perpendicular case and lower bandgap for the parallel case determine the common bandgap of all bulk modes, we consider the SPP modes that cross these two common bandgaps and discuss their dispersion features. Then, by applying the Sommerfeld integral model proposed in Section III for $h \to \infty$, the field profile of SPP waves propagating on the interface of the half-space magnetized plasma configuration is studied. Lastly, SPPs excited on the surfaces of the magnetized plasma slab (h finite) are investigated by considering the effect of thickness.

A. Dispersion Properties of the SPPs

A surface mode propagating in the *xoy* plane generally possesses two wavevector components, k_x and k_y. Therefore, a 3-D surface is needed to completely describe the SPP dispersion. As shown in Fig. 3, the SPP modes form two frequency bands. The upper band passes through the upper bulk bandgap, and the lower band passes through the lower bulk bandgap. In the case of a magnetized plasma-opaque material (such as metal as the upper region), the upper band of SPP modes are topological, unidirectional, and backscattering immune SPPs which have been well studied in [7], [14], [17], [19], and [20]. For the case that the magnetized plasma is covered by a transparent medium as considered here, the upper band represents fast surface waves (leaky waves); only the real part of the frequency is shown in Fig. 3(a). These surface waves leak rapidly into the transparent medium. There is a small break in the upper band, as we were able to find roots for very small values of k_x but not exactly at $k_x = 0$ (i.e., when propagation is exactly along the bias). However, the lower band is the main interest here, and dispersion in this lower band leads to beam-like SPPs, which have only recently been considered [21]–[23]; this is the main subject of this work.

Fig. 4 shows several equi-frequency contours (EFCs) of the dispersion surface at different frequencies (red lines). Also shown in Fig. 4 are density plots of the scattered field integrand in (14), in which $h \to \infty$ (single interface configuration).

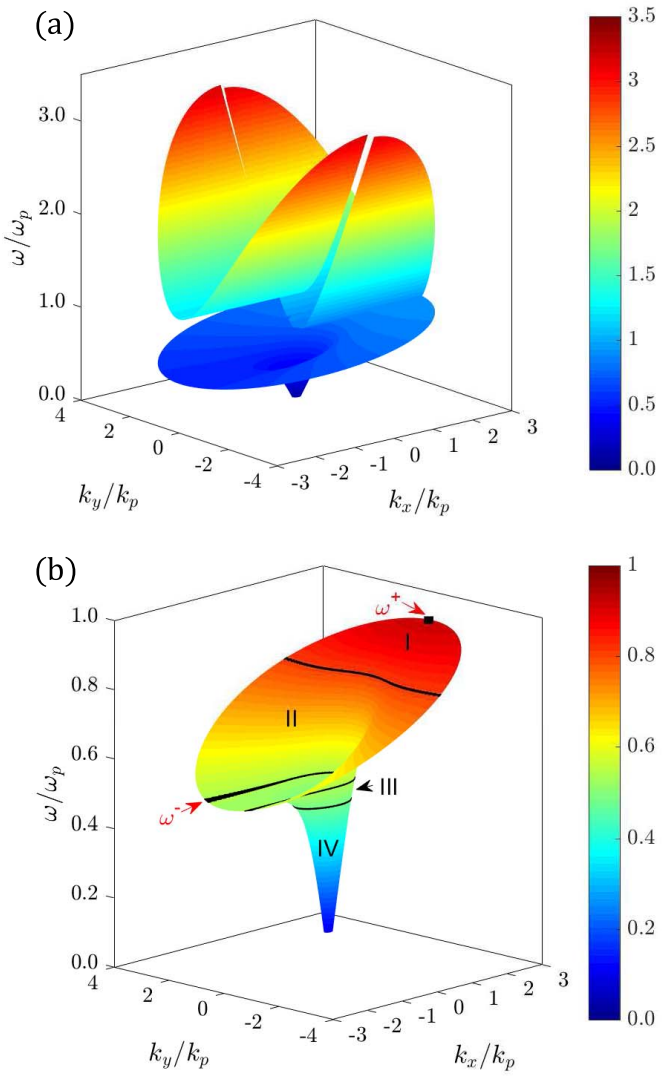

Fig. 3. SPP dispersion surface for a biased-plasma–vacuum interface, obtained by solving for the roots of (10). (a) Perspective view of the upper and lower bands. The upper band are for fast (leaky) waves, and the real part of the frequency is shown. (b) Close-up of the lower band, where the solid black lines are the EFCs for a few representative frequencies and $\omega^{\pm}$ outline the region of SPP resonance. The designations I-IV refer to Fig. 5. The common bulk bandgap is in Regions II and III.

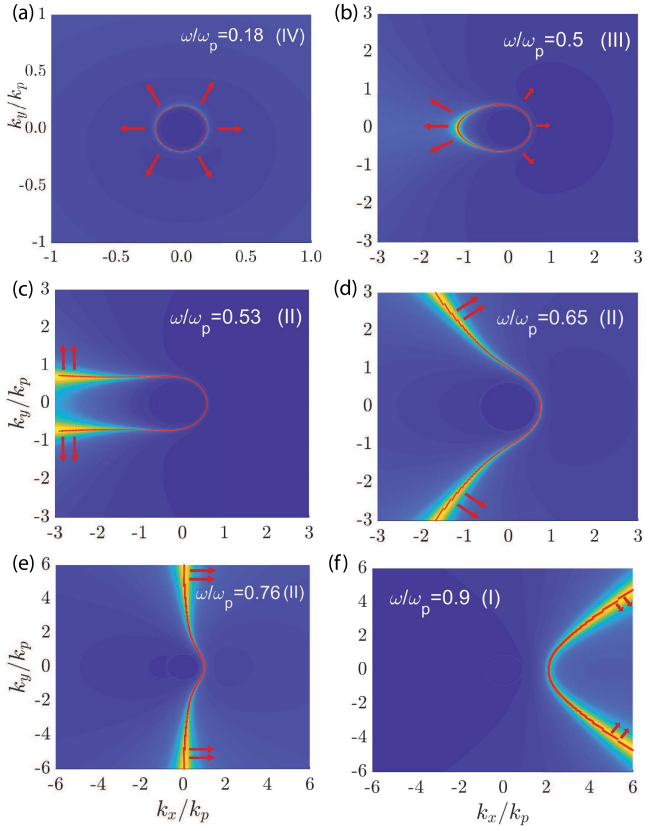

Fig. 4. Density plot of the scattered field integrand in (14), and EFCs (red solid line), extracted from (10), for a half-space biased-plasma medium at different frequencies. The notation I-IV refers to the regions shown in Fig. 5. Red arrows indicate the direction of the group velocity vectors. (a) $\omega/\omega_p = 0.18$. (b) $\omega/\omega_p = 0.5$. (c) $\omega/\omega_p = 0.53$. (d) $\omega/\omega_p = 0.65$. (e) $\omega/\omega_p = 0.76$. (f) $\omega/\omega_p = 0.9$.

The phase and group velocities of an SPP are calculated as $\mathbf{v}_p = \hat{\mathbf{k}}_s \omega/|\mathbf{k}_s|$ and

$$\mathbf{v}_g = \nabla_{\mathbf{k}s}\omega(\mathbf{k}_s) = \hat{\mathbf{x}}\frac{\partial\omega}{\partial k_x} + \hat{\mathbf{y}}\frac{\partial\omega}{\partial k_y}, \tag{20}$$

respectively. This means that the group velocity, representing the directional flow of electromagnetic energy in the lossless case, is orthogonal to the EFCs. The direction of the group velocity vectors are shown in Fig. 4 by red arrows. According to Fig. 4(a), the EFCs at low frequencies are nearly circular, such that energy flows almost isotropically. Hence, the resulting field pattern is essentially omnidirectional. As frequency increases, the semi-major axis of the EFC becomes elongated [see Fig. 4(b)] such that the energy begins to flow asymmetrically. For $\omega = 0.53\omega_p$, the EFC becomes hyperbolic-like, with the arms of the curve widening as frequency increases [see Fig. 4(c)–(e)] and then flipping direction [see Fig. 4(f)]. The hyperbolic-like EFC of the lower SPP band results in narrow SPP beams. For the cases where narrow beams are formed [see Fig. 4(c)–(f)], the group velocity vectors point along the beam directions. Because of the near-flat dispersion shown in Fig. 5, discussed next, the group velocity is a small fraction of the speed of wave in vacuum (less than $0.05c$, where c is the speed of light), representing very slow surface waves.

Fig. 5(a) shows the SPP dispersion behavior for the lower SPP band, at different propagation angles [i.e., it shows several two-dimensional traces of the SPP dispersion surface shown in Fig. 3(b)]. Each branch of the SPP dispersion converges to (19) in the limit $k_s = |\mathbf{k}_s| \to \infty$, derived using the quasi-static approximation for the plasma half-space. The maximum and minimum quasi-static resonance, $\omega^{\pm} = \omega_k(\phi_s = 0, \phi_s = 180°)$, indicated in Figs. 3(b) and 5(a), correspond to an SPP mode which propagates perpendicular to the bias. In Fig. 5(a), the bulk dispersion for $\alpha_b = 0°$ (black solid lines) indicates the common bulk bandgap that the SPPs in the lower SPP band cross. The dispersion is divided into four frequency regions: in Regions I and IV, there is no common bulk bandgap, whereas in Regions II and III, there exists a common bulk bandgap. In Region II, where the EFC is hyperbolic like [see Fig. 4(c)–(f)], we have directional propagation and the

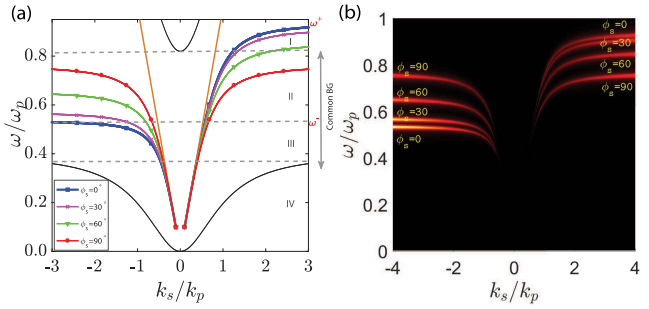

Fig. 5. (a) 2-D dispersion of the SPP for different propagation angles, ϕ_s, with respect to the positive (negative) x-axis for right (left) branches of the dispersion. The bulk dispersion (black solid lines) for $\alpha_b = 0°$ indicates the lower bulk bandgap common to all propagation angles. The solid orange lines show the dispersion of light in vacuum, e.g., $\omega/\omega_p = \pm k_s/k_p$. (b) Density plot of the scattered field integrand in (14) in the $\omega - k_s$ plane. The bright parts correspond to the flat parts of the 2-D dispersion curves in (a), representing the dominant contribution to the narrow beams.

SPP field pattern consists of two narrow beams which are symmetric with respect to the x-axis, and since $\omega(-\mathbf{k}_s) \neq \omega(\mathbf{k}_s)$, unidirectional behavior is also possible, making this frequency regime of central interest. Although in Region III there still exists a common bulk bandgap, narrow beams do not form in the SPP field pattern due to the fact that the EFC is ellipsoidal [see Fig. 4(b)]. In Region IV, the EFC is nearly circular [see Fig. 4(a)], indicating that the SPP field pattern is approximately omnidirectional. Similar to Fig. 4, the density plot of the scattered electric field integrand in (14) is shown in Fig. 5(b) for different SPP angles. The brightest parts correspond to the flat parts of the dispersion curve in Fig. 5(a). This means that for a given frequency in region (II), the flat part coincident with the ω = constant line has the most contribution in forming the narrow beams discussed and gives insight into the group velocity of the beam.

B. SPPs at the Interface of a Half-Space Gyrotropic Medium

Considering a half-space gyrotropic medium, a vertical dipole source at $(\rho, z) = (0, 0)$ excites SPPs at the interface. To obtain the electric field distribution of SPP waves due to the vertical dipole source, we apply the the Green function model (14) for $h \to \infty$, derived in Section III as well as finite element modeling using COMSOL. The scattered fields near the interface for several frequencies that lie in the four regions shown in Fig. 5 and for radial distance $\rho = 0.7\lambda$, height $z = 0.016\lambda_p$, and $0 < \varphi < 2\pi$, calculated using the Sommerfeld integral, are shown as the polar patterns in Fig. 6(b), (d), and (f). The electric field distribution at the *xoy* plane obtained in COMSOL are shown in Fig. 6(a), (c), and (e), and agree with the Green function analysis. As shown in Fig. 6(a) and (b), the expected behavior of surface wave propagation for operating frequencies that lie in Region IV of the dispersion (see Figs. 3 and 5) is nearly omnidirectional. In Region III, propagation is bidirectional, with the SPP intensity concentrated to one half-plane, as shown in Fig. 6(c) and (d). As frequencies change from lying in Region IV to Regions II and I of Fig. 5, the SPP increasingly tends toward being unidirectional.

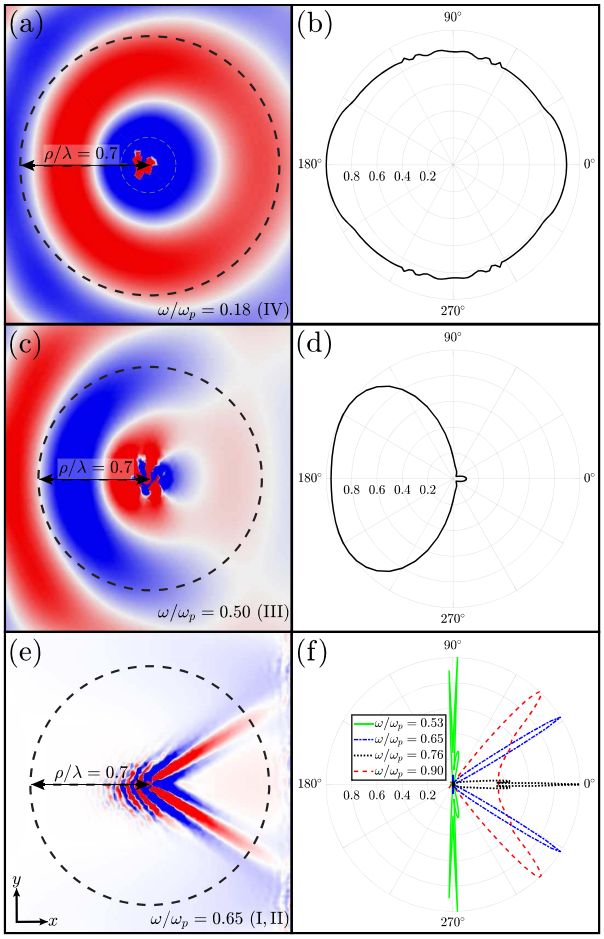

Fig. 6. (a), (c), and (e) Electric field distribution in the *xoy* plane generated using COMSOL. The dashed circle of radius $\rho = 0.7\lambda$ indicates the spatial contour over which the Green function results in the right panels are shown. (b), (d), and (f) Polar patterns of the scattered electric field, $|E_z^r|$, obtained from the Green function for a magnetized plasma-vacuum interface, $(\rho, z, \varphi) = (0.7\lambda,\ 0.016\lambda_p,\ 0 < \varphi < 2\pi)$, and $= 0.015\omega_p$. The panel dimensions are $2\lambda \times 2\lambda$. (f) Results for several values of frequency, whereas the corresponding (e) is for one of the frequencies in (f). λ is free space wavelength and $\lambda_p = 2\pi c/\omega_p$.

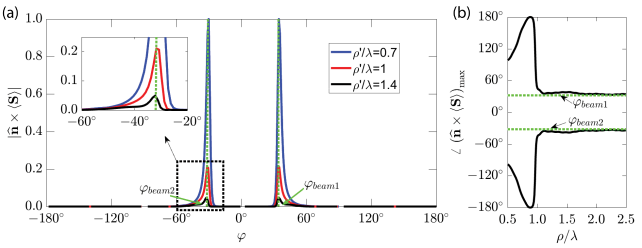

Fig. 7. Poynting vector. (a) Absolute value of tangential Poynting vector for observation points on circles with different radii, $(\rho, z, \varphi) = (\rho', 0.016\lambda_p, -\pi < \varphi < \pi)$. (b) Direction of maximum Poynting vector for observation points along the two main narrow beams, $(\rho, z, \varphi) = (\rho, 0.016\lambda_p, \varphi_{beam1,2} = \pm 32°)$. $\hat{\mathbf{n}}$ is the unit normal vector to the interface. The dashed lines show the beam angles, and it is seen that the Poynting vector becomes aligned with the beam angle, as expected, for observation points not too close to the source. The operating and collision frequency are $\omega = 0.65\omega_p$ and $\Gamma = 0.015\omega_p$, respectively.

Interestingly, for frequencies that satisfy the SPP resonant condition, $\omega^- < \omega < \omega^+$ (Regions I and II), Fig. 6(e) and (f), show that narrow-beam directional propagation is obtained,

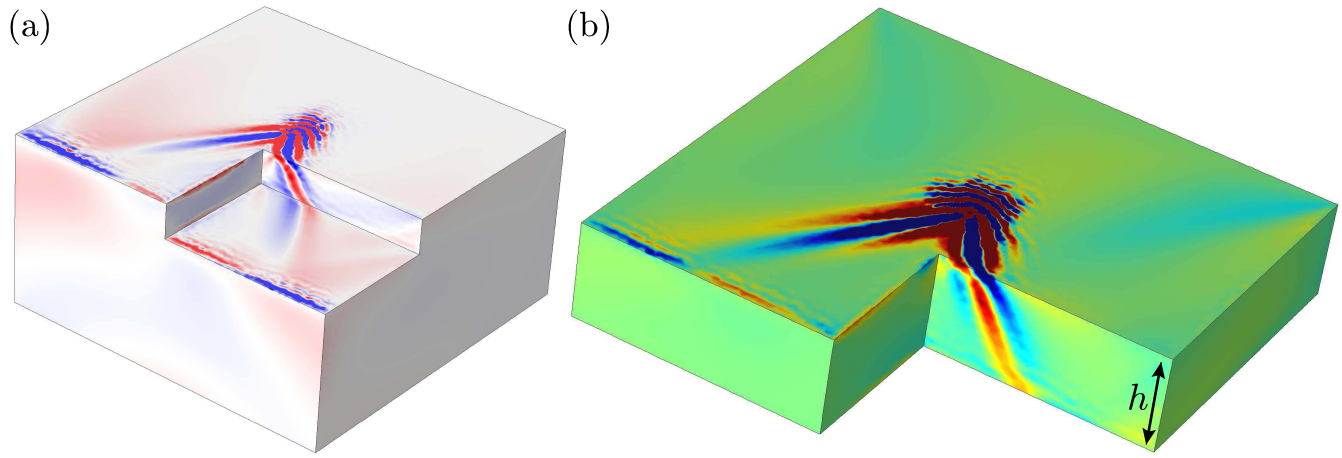

Fig. 8. (a) Electric field distribution (E_z) computed using COMSOL at the interface of a half-space gyrotropic plasma in the presence of a hole discontinuity. (b) Electric field distribution (E_z) computed using COMSOL at the interface of a finite thickness slab ($h = 0.12\lambda_p$) in the presence of a discontinuity; the SPP, excited on the top interface by a point dipole, propagates around the open surface to the bottom side of the plasma. $\Gamma = 0.04\omega_p$.

consistent with the previous discussion of EFCs. As shown in the polar pattern of Fig. 6(f), at $\omega = \omega^- = 0.53\omega_p$, the field pattern forms two narrow beams which approach each other as the operating frequency increases. Eventually, the two beams join to form a single beam at $\omega = 0.76\omega_p$, corresponding to the saturation frequency of the $\phi_s = 90°$ branch in Fig. 5, and then split to form two beams for $0.76\omega_p < \omega < \omega^+$. Therefore, the angle of the beams with respect to the x-axis is adjustable with frequency as well as the magnetic bias. Furthermore, if the direction of the magnetic bias is flipped, the beams propagate in the opposite direction.

In what follows, we particularly consider SPPs in the resonance frequency range, $\omega^- < \omega < \omega^+$ where there are two narrow beams in the field pattern. We chose $\omega = 0.65\omega_p$, a frequency within the resonance frequency range as an example to discuss the results. At this specific frequency, there are two beams with angles $\varphi_{\text{beam1,2}} = \pm 32°$ with respect to the x-axis.

We should note that in the general lossy case, the group velocity is ill-defined as an energy-transport velocity, and one should examine the Poynting vector and energy transport velocity. In this work, we incorporate realistic material loss, but the results do not qualitatively change in the lossless case, in which case the meaning of the group velocity is very clear: it is $S_{\text{avg}}/W_{\text{stored}}$, where S_{avg} is the vertically averaged Poynting vector associated with the mode and W_{stored} is the vertically averaged stored energy density. Here we consider the group velocity as the energy transport velocity merely in the sense of the beam angle, although for quantitative values of the magnitude of the energy velocity, one should examine the Poynting vector, as discussed next.

The tangential Poynting vector indicates the power carried by the surface waves. The magnitude of the tangential Poynting vector at $\omega = 0.65\omega_p$ for a set of observation points on different circular contours in space having different radii is shown in Fig. 7(a). For each radial distance, there are two peak values which occur exactly at the position of the narrow beams, $\varphi_{\text{beam1,2}}$. Then, to find the direction of the maximum radiation power, the angle of the Poynting vector for points located along the beams is extracted [see Fig. 7(b)]. As shown, the Poynting vector angle converges to the beam angles for large radial distance, i.e. in the far-field of the source. The Poynting vector and group velocity are in the same direction, pointing along the beam angle.

The SPPs within the resonant range are robust to the presence of discontinuities. To have an indication of the inherent robustness of these SPPs, a discontinuity is constructed in an attempt to impede the SPP. A unidirectional SPP that crosses a bandgap in reciprocal space is immune to the effects of backscattering and diffraction. To illustrate this, Fig. 8(a) shows the electric field due to a electric point source near the vacuum–plasma interface of a plasma half-space. The SPP passes through the discontinuity without reflection or diffraction.

C. SPPs on Surfaces of the Magnetized Plasma Slab

For a finite thickness slab, we consider the excitation of SPPs at the first interface ($z = 0$) and the bottom interface ($z = -h$) due to a vertical dipole source positioned at the first interface ($d = 0$). Similar to single-interface configuration, the SPPs propagating on the surfaces of the plasma slab are robust to discontinuities. As shown in Fig. 8(b), upon encountering the end of the plasma, SPPs pass onto the bottom surface without reflection or diffraction. In Figs. 6 and 8, to obtain convergence in COMSOL, the material loss had to be increased, and values $0.015\omega_p < \Gamma \leq 0.06\omega_p$ were used, although it is important to note that the value of loss does not affect the beam direction.

Fig. 9(a)–(e) show how the beams at the upper interface evolve with slab thickness for a set observation point $(\rho, z, \varphi) = (0.5\lambda, 0.03\lambda, 0 < \varphi < 2\pi)$ and thickness values that fall within the range $0 < h < 0.3\lambda_p$. The frequency of operation is set within the bulk bandgap of the plasma, $\omega = 0.65\omega_p$, and the collision frequency is set to $\Gamma = 0.015\omega_p$. The values of thickness considered in Fig. 9(a)–(d) are (a) $h = 0.3\lambda_p$, (b) $h = 0.1\lambda_p$, (c) $h = 0.07\lambda_p$, and (d) $h = 0.045\lambda_p$. Each pattern is normalized with respect to the beam maximum obtained for a thick

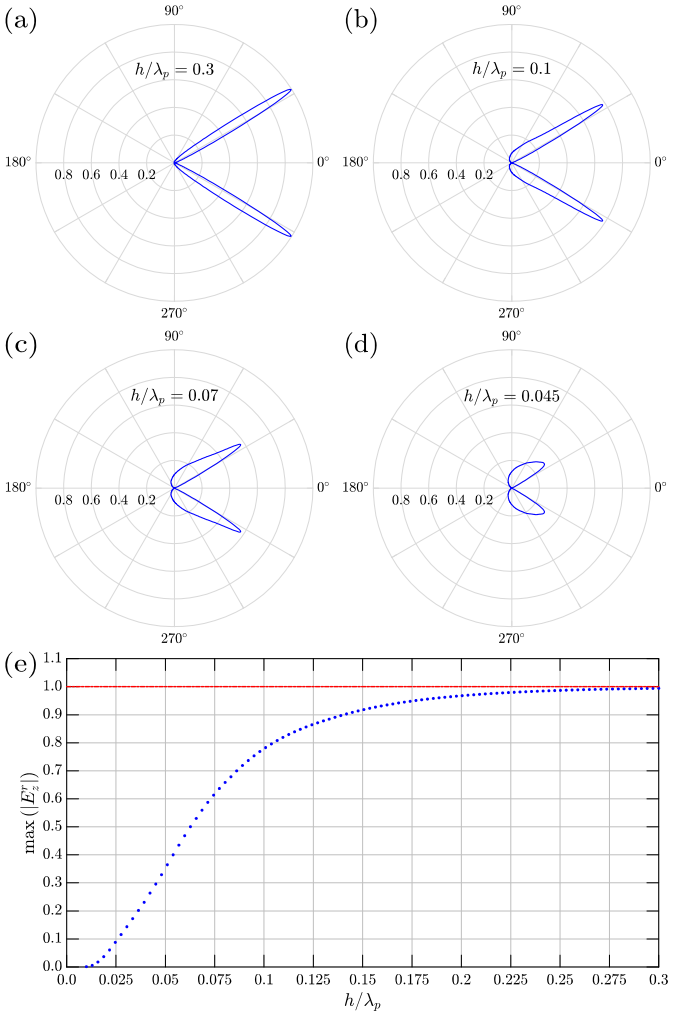

Fig. 9. SPP beam pattern excited by a vertical dipole source at the first interface of a finite thickness biased-plasma slab obtained by evaluating (14) for set observation point $(\rho, z, \varphi) = (0.5\lambda, 0.03\lambda, 0 < \varphi < 2\pi)$ where λ denotes the free space wavelength. The frequency of operation is set within the bulk bandgap of the plasma $\omega = 0.65\omega_p$ and the collision frequency is set to $\Gamma = 0.015\omega_p$. Four values of thickness are considered such that (a) $h = 0.3\lambda_p$, (b) $h = 0.1\lambda_p$, (c) $h = 0.07\lambda_p$, and (d) $h = 0.045\lambda_p$. These results are normalized with respect to the beam maximum, $\max\{|E_z^r|\} = 5 \times 10^{14}$ V/m, obtained for a thick slab in the limit $h \to \infty$, assuming the magnitude of the electric current dipole $J_0 = 1$ A · m. (e) The beam grows logistically as thickness increases.

slab, $|E_z^r|_{\max} = 5 \times 10^{14}$ V/m, in the limit $h \to \infty$, assuming the magnitude of the electric current dipole is $J_0 = 1$ A · m, where $J_0 = -j\omega p_z$ and p_z is the electric dipole moment. In Fig. 9(e), it is shown that the beam maximum grows logistically with thickness and asymptotically approaches the thick slab result as thickness increases.

When the slab becomes thin enough, it is also possible that a source on the upper interface excites SPPs on the bottom interface. The two bottom-surface SPP beams are in the opposite direction of the SPP beams on the top interface. Fig. 10(a) and (b) shows the squared amplitude of the electric field at the bottom interface ($z = -h$) and top interface ($z = 0$) obtained using the FEM method in COMSOL, while Fig. 10(c) and (d) show the squared amplitude of the transmitted and reflected field obtained by

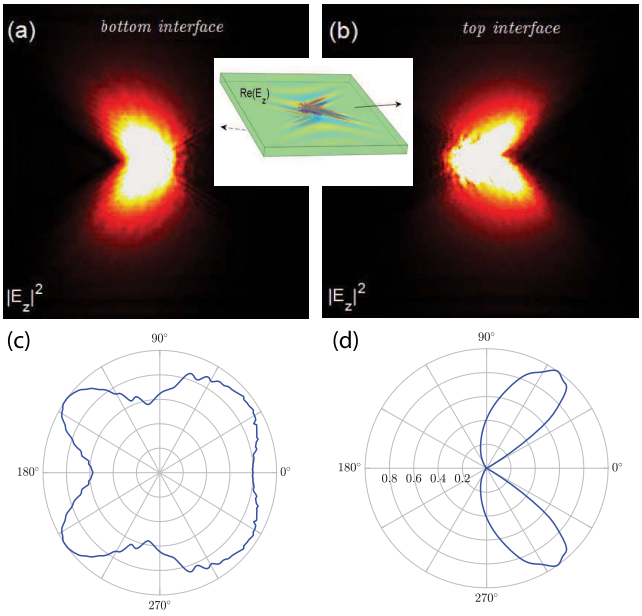

Fig. 10. Squared amplitude of the scattered electric field profile (z component) excited by a vertical dipole source located at the first interface ($d = 0$) of a thin finite thickness biased-plasma slab of thickness $h = 0.04\lambda_p$. (a) and (b) Squared amplitudes of the scattered electric field below and above the slab are obtained using COMSOL ($\Gamma = 0.05\omega_p$) and in (c) and (d) by evaluating the Sommerfeld integrals in (14) and (15). In (c), the observation point is chosen to be $z = -h - 0.1\lambda$, $\rho = 0.9\lambda$, and $0 < \varphi < 2\pi$, and in (d) the observation point is chosen to be $z = 0.03\lambda$, $\rho = 0.5\lambda$, and $0 < \varphi < 2\pi$, and $\Gamma = 0.015\omega_p$. The operating frequency is $\omega = 0.65\omega_p$.

evaluating (15) and (14), respectively, for a small distance below and above the slab. For a thin slab, there are two forward beams on the top interface and two backward beams on the bottom interface. To find the evidence of them from the dispersion diagram, the quasi-static approach for magnetized plasma slab is used. Fig. 11 shows the solutions to the quasi-static relation (17) for magnetized plasma slab with thickness of $h = 0.25\lambda_p$ and for several values of cyclotron frequency, representing the SPP resonance in the quasi-static limit. For a given ω value, there are four values of ϕ_s, two of which correspond to the forward beams on the top interface and the other two correspond to the backward beams on the bottom interface. This suggests that four beams may be present in the scattered field profile for operating frequencies that fall within the SPP resonant range $\omega^- < \omega < \omega^+$. For example, consider an operating frequency of $\omega = 0.65\omega_p$ and cyclotron frequency $\omega_c = 0.4\omega_p$; from the quasi-static dispersion, we find that the in-plane wavevector, and hence, phase velocity, of the SPP (approximately) makes an angle $\phi_s \in \{58°, 122°, 238°, 302°\}$, with respect to the x-axis. The group velocity (i.e., the direction of energy flow as indicated by the direction of the beams for the lossless case) of the SPP is perpendicular to the phase velocity and therefore, makes an angle $\phi_s \pm 90° \in \{148°, 32°, 328°, 212°\}$, with respect to the x-axis. The scattered field profile shows four beams with the expected angles with respect to the x-axis. Two forward beams are present on the top interfaces at angles $\{32°, 328°\}$ and two backward beams on the bottom

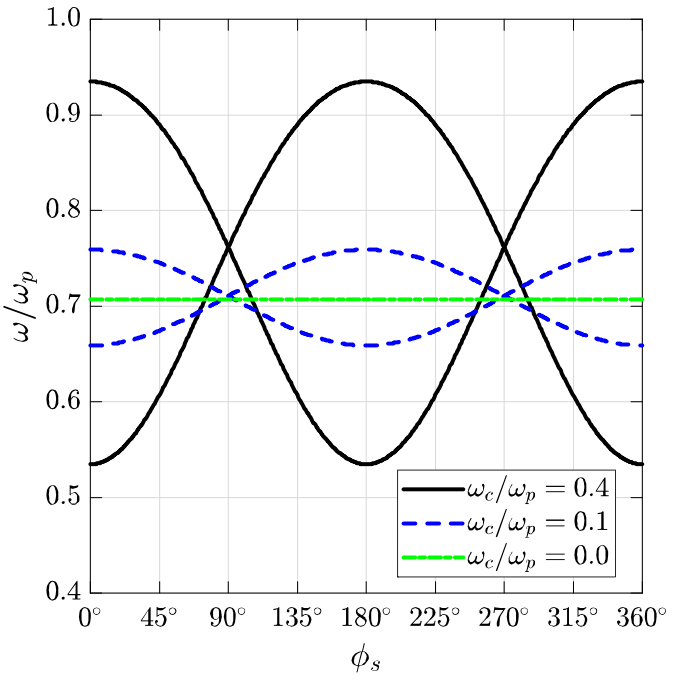

Fig. 11. Solutions to the quasi-static SPP dispersion relation (17) for a finite thickness slab of thickness $h = 0.25\lambda_p$ and wavenumber $k_s = 10k_p \gg 1/h$. The cyclotron frequency ranges from 0 to $0.4\omega_p$. From these results, we find that for a given operation frequency, a maximum of four beams is possible in the SPP beam pattern. Additionally, we find that as magnetic bias increases, the SPP resonant range also increases.

interfaces at angles $\{148°, 212°\}$. That is, the quasi-static analysis provides four symmetric beams, two of which will be excited on a given interface (top or bottom).

Furthermore, in the presence of a magnetic bias, the SPP resonance depends on the direction of the SPP modes, however, it is independent of the slab thickness for large values of k_s. As the magnetic bias tends toward zero ($\omega_c \to 0$), the SPP resonance becomes a flat curve, which means the SPP resonance is direction independent, $\lim_{\omega_c \to 0} \omega_{\text{SPP}} = \omega_p/\sqrt{2}$.

VI. Conclusion

In this work, we have investigated the behavior of SPPs propagating at the interface between air and gyrotropic plasma for both single-interface and finite-thickness biased-plasma slab configurations. We have identified a bulk bandgap, common to all propagation angles. The operating frequency is chosen to lie within the lower common bandgap, wherein omnidirectional, bidirectional, and narrow directional SPP beam patterns are observed. Operating in the bandgap gives the SPP interesting properties that protect it from backscatter and diffraction in the presence of a discontinuity. The direction of the SPP beams is adjustable with operation frequency and also the bias magnetic field. The Green function and quasi-static approximation to the dispersion have also been obtained for a finite-thickness slab.

Appendix

The incident field excited by an electric dipole source, with dipole moment $\mathbf{p} = \hat{\mathbf{x}}p_x + \hat{\mathbf{y}}p_y + \hat{\mathbf{z}}p_z$, suspended a distance

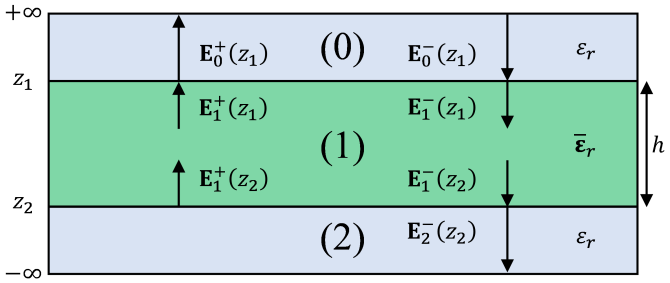

Fig. 12. Cross-sectional view of Fig. 1. The top and bottom interfaces are positioned at $z = z_1 = 0$ and $z = z_2 = -h$, respectively. Regions 0 and 2 are characterized by ε_r while Region 1 is characterized by the gyrotropic permitivitty tensor, $\bar{\varepsilon}_r$, defined in (1). The electric fields associated with plane waves propagating in each region, with group velocity in the $\pm z$ directions, are also shown.

d above the first interface, is given by $\mathbf{E}^p(\mathbf{r}) = (\nabla\nabla + \bar{\mathbf{I}}k_0^2\varepsilon_r) \cdot \pi^p(\mathbf{r})$, where $\pi^p(\mathbf{r})$ denotes the principal hertzian potential due to the dipole source, which we write in terms of the principal Green function, $\pi^p(\mathbf{r}) = g^p(\mathbf{r}, \mathbf{r}_0)\mathbf{p}/\varepsilon_0\varepsilon_r$, where $g^p(\mathbf{r}, \mathbf{r}_0) = e^{ik_0\sqrt{\varepsilon_r}|\mathbf{r}-\mathbf{r}_0|}/4\pi|\mathbf{r}-\mathbf{r}_0|$ such that ε_r is the relative permitivitty of the regions above and below the slab (see Fig. 1) and $\mathbf{r}_0 = (0, 0, d)$. Following [21], the principal and scattered fields may be written in the Fourier transform domain with respect to k_x and k_y:

$$\mathbf{E}^r(\mathbf{r}) = \int d^2\mathbf{k}_s e^{i\mathbf{k}_s\cdot(\mathbf{r}-\mathbf{r}_0)} \frac{e^{-\gamma_0(d+z)}}{8\pi^2\varepsilon_0\varepsilon_r\gamma_0} \bar{\mathbf{C}}^r \cdot \mathbf{p} \tag{21}$$

$$\mathbf{E}^t(\mathbf{r}) = \int d^2\mathbf{k}_s e^{i\mathbf{k}_s\cdot(\mathbf{r}-\mathbf{r}_0)} \frac{e^{-\gamma_0(d-z)}}{8\pi^2\varepsilon_0\varepsilon_r\gamma_0} \bar{\mathbf{C}}^t \cdot \mathbf{p} \tag{22}$$

where

$$\bar{\mathbf{C}}^r = \left(\bar{\mathbf{I}}_s - \frac{\hat{\mathbf{z}}k_s}{i\gamma_0}\right) \cdot \bar{\mathbf{R}} \cdot \left(k_0^2\varepsilon_r\bar{\mathbf{I}}_s - \mathbf{k}_s\mathbf{k}_s + i\gamma_0\mathbf{k}_s\hat{\mathbf{z}}\right) \tag{23}$$

$$\bar{\mathbf{C}}^t = \left(\bar{\mathbf{I}}_s + \frac{\hat{\mathbf{z}}k_s}{i\gamma_0}\right) \cdot \bar{\mathbf{T}} \cdot \left(k_0^2\varepsilon_r\bar{\mathbf{I}}_s - \mathbf{k}_s\mathbf{k}_s + i\gamma_0\mathbf{k}_s\hat{\mathbf{z}}\right) \tag{24}$$

such that $\bar{\mathbf{I}}_s = \hat{\mathbf{x}}\hat{\mathbf{x}} + \hat{\mathbf{y}}\hat{\mathbf{y}}$ and $\gamma_0 = \sqrt{k_x^2 + k_y^2 - k_0^2\varepsilon_r}$.

In what follows, we derive the plane wave reflection and transmission coefficients, $\bar{\mathbf{R}}(\omega, \mathbf{k}_s)$ and $\bar{\mathbf{T}}(\omega, \mathbf{k}_s)$, which relate the tangential field components of the electric field reflected and transmitted from a gyrotropic slab of finite thickness, as shown in Fig. 12. As in [21], it is important to define a convenient, orthogonal coordinate system in which to expand the amplitude vector of a plane wave propagating in the gyrotropic medium. The set of orthogonal unit vectors which span this coordinate system is given by $\{\hat{\mathbf{k}}_{t,j}^{\pm}, \hat{\mathbf{y}}, \hat{\mathbf{k}}_{t,j}^{\pm} \times \hat{\mathbf{y}}\}$, where $\hat{\mathbf{k}}_{t,j}^{\pm} = \hat{\mathbf{x}}k_x \pm \hat{\mathbf{z}}i\gamma_j$ for $j \in \{1, 2\}$. The fields above and below the interface are expanded in terms of the Cartesian basis $\{\hat{\mathbf{x}}, \hat{\mathbf{y}}, \hat{\mathbf{z}}\}$. The relationship between the tangential electric and magnetic fields in the structure is

$$\begin{pmatrix} \omega\mu_0 H_y^{\pm} \\ \omega\mu_0 H_x^{\pm} \end{pmatrix} = \{\bar{\mathbf{Y}}^{\pm}, \bar{\mathbf{Y}}_g^{\pm}\} \cdot \begin{pmatrix} E_x^{\pm} \\ E_y^{\pm} \end{pmatrix} \tag{25}$$

where $\bar{\mathbf{Y}}^{\pm}$ relates the electric and magnetic fields in the dielectric regions above and below the slab, and $\bar{\mathbf{Y}}_g^{\pm}$ relates

the electric and magnetic fields within the slab. These tensors are given by

$$\bar{\mathbf{Y}}^{\pm} = \frac{\pm 1}{i\gamma_0}\begin{pmatrix} k_x^2-\gamma_0^2 & k_xk_y \\ -k_xk_y & \gamma_0^2-k_y^2 \end{pmatrix} \tag{26}$$

$$\bar{\mathbf{Y}}_g^{\pm} = \begin{pmatrix} -\delta_1 k_{t,1}^2 & -\delta_2 k_{t,2}^2 \\ k_y\phi_1^{\pm} & k_y\phi_2^{\pm} \end{pmatrix}\cdot\begin{pmatrix} \beta_1^{\pm} & \beta_2^{\pm} \\ k_y\theta_1 & k_y\theta_2 \end{pmatrix}^{-1}. \tag{27}$$

Matching the tangential components of the electric and magnetic fields at each interface, we obtain

$$(\bar{\mathbf{I}}_s + \bar{\mathbf{R}}_{01})\cdot\mathbf{E}_0^-(z_1) = \bar{\mathbf{T}}_{01}\cdot\mathbf{E}_0^-(z_1) \tag{28}$$

$$(\bar{\mathbf{I}}_s + \bar{\mathbf{R}}_{10})\cdot\mathbf{E}_1^+(z_1) = \bar{\mathbf{T}}_{10}\cdot\mathbf{E}_1^+(z_1) \tag{29}$$

$$(\bar{\mathbf{I}}_s + \bar{\mathbf{R}}_{12})\cdot\mathbf{E}_1^-(z_2) = \bar{\mathbf{T}}_{12}\cdot\mathbf{E}_1^-(z_2) \tag{30}$$

$$(\bar{\mathbf{Y}}^- + \bar{\mathbf{Y}}^+\cdot\bar{\mathbf{R}}_{01})\cdot\mathbf{E}_0^-(z_1) = \bar{\mathbf{Y}}_g^-\cdot\bar{\mathbf{T}}_{01}\cdot\mathbf{E}_0^-(z_1) \tag{31}$$

$$(\bar{\mathbf{Y}}_g^+ + \bar{\mathbf{Y}}_g^-\cdot\bar{\mathbf{R}}_{10})\cdot\mathbf{E}_1^+(z_1) = \bar{\mathbf{Y}}^+\cdot\bar{\mathbf{T}}_{10}\cdot\mathbf{E}_1^+(z_1) \tag{32}$$

$$(\bar{\mathbf{Y}}_g^- + \bar{\mathbf{Y}}_g^+\cdot\bar{\mathbf{R}}_{12})\cdot\mathbf{E}_1^-(z_2) = \bar{\mathbf{Y}}^-\cdot\bar{\mathbf{T}}_{12}\cdot\mathbf{E}_1^-(z_2) \tag{33}$$

where

$$\bar{\mathbf{R}}_{nn'} = \left(\bar{\mathbf{Y}}^{m_1} - \bar{\mathbf{Y}}_g^{m_2}\right)^{-1}\cdot\left(\bar{\mathbf{Y}}_g^{m_3} - \bar{\mathbf{Y}}^{m_3}\right) \tag{34}$$

such that

$$(m_1,m_2,m_3) = \begin{cases} (+,-,-), & (n,n') = (0,1) \\ (+,-,+), & (n,n') = (1,0) \\ (-,+,-), & (n,n') = (1,2) \end{cases} \tag{35}$$

and from (28)–(33), it follows that $\bar{\mathbf{T}}_{nn'} = \bar{\mathbf{I}}_s + \bar{\mathbf{R}}_{nn'}$. Furthermore, it is important to note the relations

$$\mathbf{E}_1^-(z_1) = \bar{\mathbf{T}}_{01}\cdot\mathbf{E}_0^-(z_1) + \bar{\mathbf{R}}_{10}\cdot\mathbf{E}_1^+(z_1) \tag{36}$$

$$\mathbf{E}_0^+(z_1) = \bar{\mathbf{R}}_{01}\cdot\mathbf{E}_0^-(z_1) + \bar{\mathbf{T}}_{10}\cdot\mathbf{E}_1^+(z_1) \tag{37}$$

$$\mathbf{E}_1^+(z_2) = \bar{\mathbf{R}}_{12}\cdot\mathbf{E}_1^-(z_2) \tag{38}$$

$$\mathbf{E}_2^-(z_2) = \bar{\mathbf{T}}_{12}\cdot\mathbf{E}_1^-(z_2) \tag{39}$$

where the electric field associated with a plane wave propagating a distance, $h = |z_2 - z_1|$, along the $\pm z$ direction within the gyrotropic slab, is given by

$$\mathbf{E}_1^+(z_1) = \bar{\mathbf{P}}^+\cdot\mathbf{E}_1^+(z_2) \tag{40}$$

$$\mathbf{E}_1^-(z_2) = \bar{\mathbf{P}}^-\cdot\mathbf{E}_1^-(z_1) \tag{41}$$

where $\bar{\mathbf{P}}^{\pm}$ denotes the spacial propagator that effectively propagates the electric field a distance h through the slab and takes the form

$$\bar{\mathbf{P}}^{\pm} = \bar{\mathbf{U}}_{\pm}\cdot\bar{\mathbf{P}}\cdot\bar{\mathbf{U}}_{\pm}^{-1} \tag{42}$$

where

$$\bar{\mathbf{U}}_{\pm} = \begin{pmatrix} \beta_1^{\pm}/k_{t,1} & \beta_2^{\pm}/k_{t,2} \\ k_y\theta_1/k_{t,1} & k_y\theta_2/k_{t,2} \end{pmatrix} \tag{43}$$

$$\bar{\mathbf{P}} = \begin{pmatrix} e^{-\gamma_1 h} & 0 \\ 0 & e^{-\gamma_2 h} \end{pmatrix}. \tag{44}$$

Using (40) and (41) in (36)–(39) leads to

$$\mathbf{E}_0^+(z_1) = \bar{\mathbf{R}}\cdot\mathbf{E}_0^-(z_1) \tag{45}$$

$$\mathbf{E}_2^-(z_2) = \bar{\mathbf{T}}\cdot\mathbf{E}_0^-(z_1) \tag{46}$$

where

$$\bar{\mathbf{R}} = \bar{\mathbf{R}}_{01} + \bar{\mathbf{T}}_{10}\cdot\bar{\mathbf{R}}'_{12}\cdot(\bar{\mathbf{I}}_s - \bar{\mathbf{R}}_{10}\cdot\bar{\mathbf{R}}'_{12})^{-1}\cdot\bar{\mathbf{T}}_{01} \tag{47}$$

$$\bar{\mathbf{T}} = \bar{\mathbf{T}}_{12}\cdot\bar{\mathbf{P}}^-\cdot\left(\bar{\mathbf{I}}_s - \bar{\mathbf{R}}_{10}\cdot\bar{\mathbf{R}}'_{12}\right)^{-1}\cdot\bar{\mathbf{T}}_{01} \tag{48}$$

such that $\bar{\mathbf{R}}'_{12} = \bar{\mathbf{P}}^+\cdot\bar{\mathbf{R}}_{12}\cdot\bar{\mathbf{P}}^-$. Finally, after some algebra, it can be shown that (34), (42), (47), and (48) may be written in quotient form as

$$\bar{\mathbf{R}}_{nn'} = \frac{1}{\Omega^{nn'}}\begin{pmatrix} \Pi_{11}^{nn'} & \Pi_{12}^{nn'}/k_y \\ k_y\Pi_{21}^{nn'} & \Pi_{22}^{nn'} \end{pmatrix} \tag{49}$$

$$\bar{\mathbf{P}}^{\pm} = \frac{1}{\chi^{\pm}}\begin{pmatrix} \Delta_{11}^{\pm} & \Delta_{12}^{\pm}/k_y \\ k_y\Delta_{21}^{\pm} & \Delta_{22}^{\pm} \end{pmatrix} \tag{50}$$

$$\bar{\mathbf{R}} = \frac{1}{\Lambda\Omega^{01}}\begin{pmatrix} \Xi_{11} & \Xi_{12}/k_y \\ k_y\Xi_{21} & \Xi_{22} \end{pmatrix} \tag{51}$$

$$\mathbf{T} = \frac{\Omega^{10}\chi^+}{\Lambda\Omega^{01}}\begin{pmatrix} \Psi_{11} & \Psi_{12}/k_y \\ k_y\Psi_{21} & \Psi_{22} \end{pmatrix} \tag{52}$$

where

$$\begin{aligned}\Omega^{nn'} &= m_1m_3\gamma_0\chi^{m_3}\left(Q_E^{m_2} - \varepsilon_r\chi^{m_2}\right) \\ &\quad + m_3\chi^{m3}\left[\left(k_y^2-\gamma_0^2\right)Q_A + k_xk_y^2Q_C^{m_2}\right] \\ &\quad - m_3\chi^{m3}\left[\left(k_x^2-\gamma_0^2\right)Q_D^{m_2} + k_xQ_B^{m_2}\right] \end{aligned}\tag{53}$$

$$\begin{aligned}\Pi_{11}^{nn'} &= \gamma_0\left[\varepsilon_r\chi^{m_2}\chi^{m_3} + m_1m_3k_0^2\left(Q_AQ_D^{m_2} - Q_C^{m_3}Q_B^{m_2}\right)\right] \\ &\quad - m_3\chi^{m_2}\left[\left(k_y^2-\gamma_0^2\right)Q_A + k_xk_y^2Q_C^{m_3}\right] \\ &\quad + m_1\chi^{m_3}\left[\left(k_x^2-\gamma_0^2\right)Q_D^{m_2} + k_xQ_B^{m_2}\right] \end{aligned}\tag{54}$$

$$\begin{aligned}\Pi_{12}^{nn'} &= m_1m_3\gamma_0k_0^2\left(Q_D^{m_2}Q_B^{m_3} - Q_D^{m_3}Q_B^{m_2}\right) \\ &\quad + k_xk_y^2\left(m_1\chi^{m_3}Q_D^{m_2} - m_3\chi^{m_2}Q_D^{m_3}\right) \\ &\quad + \left(k_y^2-\gamma_0^2\right)\left(m_1\chi^{m_3}Q_B^{m_2} - m_3\chi^{m_2}Q_B^{m_3}\right) \end{aligned}\tag{55}$$

$$\begin{aligned}\Pi_{21}^{nn'} &= m_1m_3\gamma_0k_0^2\left(Q_AQ_C^{m_3} - Q_AQ_C^{m_2}\right) \\ &\quad - k_x\left(m_1\chi^{m_3}Q_A - m_3\chi^{m_2}Q_A\right) \\ &\quad - \left(k_x^2-\gamma_0^2\right)\left(m_1\chi^{m_3}Q_C^{m_2} - m_3\chi^{m_2}Q_C^{m_3}\right) \end{aligned}\tag{56}$$

$$\begin{aligned}\Pi_{22}^{nn'} &= \gamma_0\left[\varepsilon_r\chi^{m_2}\chi^{m_3} + m_1m_3k_0^2\left(Q_AQ_D^{m_3} - Q_C^{m_2}Q_B^{m_3}\right)\right] \\ &\quad - m_1\chi^{m_3}\left[\left(k_y^2-\gamma_0^2\right)Q_A + k_xk_y^2Q_C^{m_2}\right] \\ &\quad + m_3\chi^{m_2}\left[\left(k_x^2-\gamma_0^2\right)Q_D^{m_3} + k_xQ_B^{m_3}\right] \end{aligned}\tag{57}$$

and

$$\begin{aligned}\Delta_{11}^{\pm} &= k_{t,1}^2\xi_1\varpi_2\alpha_2^{\pm}e^{-\gamma_{z,2}h} \\ &\quad - k_{t,2}^2\xi_2\varpi_1\alpha_1^{\pm}e^{-\gamma_{z,1}h} \end{aligned}\tag{58}$$

$$\Delta_{12}^{\pm} = \varpi_1\varpi_2\alpha_1^{\pm}\alpha_2^{\pm}\left(e^{-\gamma_{z,2}h} - e^{-\gamma_{z,1}h}\right) \tag{59}$$

$$\Delta_{21} = k_{t,1}^2k_{t,2}^2\xi_1\xi_2\left(e^{-\gamma_{z,1}h} - e^{-\gamma_{z,2}h}\right) \tag{60}$$

$$\begin{aligned}\Delta_{22}^{\pm} &= k_{t,1}^2\xi_1\varpi_2\alpha_2^{\pm}e^{-\gamma_{z,1}h} \\ &\quad - k_{t,2}^2\xi_2\varpi_1\alpha_1^{\pm}e^{-\gamma_{z,2}h} \end{aligned}\tag{61}$$

and

$$\Xi_{11} = \Lambda\Pi_{11}^{01} + \Pi_{12}^{10}(\Upsilon_{21}\Sigma_{11} + \Upsilon_{22}\Sigma_{21}) + (\Omega^{10} + \Pi_{11}^{10})(\Upsilon_{11}\Sigma_{11} + \Upsilon_{12}\Sigma_{21}) \quad (62)$$

$$\Xi_{12} = \Lambda\Pi_{12}^{01} + \Pi_{12}^{10}(\Upsilon_{21}\Sigma_{12} + \Upsilon_{22}\Sigma_{22}) + (\Omega^{10} + \Pi_{11}^{10})(\Upsilon_{11}\Sigma_{12} + \Upsilon_{12}\Sigma_{22}) \quad (63)$$

$$\Xi_{21} = \Lambda\Pi_{21}^{01} + \Pi_{21}^{10}(\Upsilon_{11}\Sigma_{11} + \Upsilon_{12}\Sigma_{21}) + (\Omega^{10} + \Pi_{22}^{10})(\Upsilon_{21}\Sigma_{11} + \Upsilon_{22}\Sigma_{21}) \quad (64)$$

$$\Xi_{22} = \Lambda\Pi_{22}^{01} + \Pi_{21}^{10}(\Upsilon_{11}\Sigma_{12} + \Upsilon_{12}\Sigma_{22}) + (\Omega^{10} + \Pi_{22}^{10})(\Upsilon_{21}\Sigma_{12} + \Upsilon_{22}\Sigma_{22}) \quad (65)$$

and

$$\Psi_{11} = \Pi_{12}^{12}(\Delta_{21}\Sigma_{11} + \Delta_{22}^{-}\Sigma_{21}) + (\Omega^{12} + \Pi_{11}^{12})(\Delta_{11}^{-}\Sigma_{11} + \Delta_{12}^{-}\Sigma_{21}) \quad (66)$$

$$\Psi_{12} = \Pi_{12}^{12}(\Delta_{21}\Sigma_{12} + \Delta_{22}^{-}\Sigma_{22}) + (\Omega^{12} + \Pi_{11}^{12})(\Delta_{11}^{-}\Sigma_{12} + \Delta_{12}^{-}\Sigma_{22}) \quad (67)$$

$$\Psi_{21} = \Pi_{21}^{12}(\Delta_{11}^{-}\Sigma_{11} + \Delta_{12}^{-}\Sigma_{21}) + (\Omega^{12} + \Pi_{22}^{12})(\Delta_{21}\Sigma_{11} + \Delta_{22}^{-}\Sigma_{21}) \quad (68)$$

$$\Psi_{22} = \Pi_{21}^{12}(\Delta_{11}^{-}\Sigma_{12} + \Delta_{12}^{-}\Sigma_{22}) + (\Omega^{12} + \Pi_{22}^{12})(\Delta_{21}\Sigma_{12} + \Delta_{22}^{-}\Sigma_{22}) \quad (69)$$

and

$$\Lambda = -\Theta_{12}\Theta_{21} + (\Omega^{10}\Omega^{12}\chi^{+}\chi^{-} - \Theta_{11})(\Omega^{10}\Omega^{12}\chi^{+}\chi^{-} - \Theta_{22}) \quad (70)$$

such that

$$\Upsilon_{11} = \Delta_{11}^{+}(\Pi_{11}^{12}\Delta_{11}^{-} + \Pi_{12}^{12}\Delta_{21}) + \Delta_{12}^{+}(\Pi_{21}^{12}\Delta_{11}^{-} + \Pi_{22}^{12}\Delta_{21}) \quad (71)$$

$$\Upsilon_{12} = \Delta_{11}^{+}(\Pi_{11}^{12}\Delta_{12}^{-} + \Pi_{12}^{12}\Delta_{22}^{-}) + \Delta_{12}^{+}(\Pi_{21}^{12}\Delta_{12}^{-} + \Pi_{22}^{12}\Delta_{22}^{-}) \quad (72)$$

$$\Upsilon_{21} = \Delta_{21}(\Pi_{11}^{12}\Delta_{11}^{-} + \Pi_{12}^{12}\Delta_{21}) + \Delta_{22}^{+}(\Pi_{21}^{12}\Delta_{11}^{-} + \Pi_{22}^{12}\Delta_{21}) \quad (73)$$

$$\Upsilon_{22} = \Delta_{21}(\Pi_{11}^{12}\Delta_{12}^{-} + \Pi_{12}^{12}\Delta_{22}^{-}) + \Delta_{22}^{+}(\Pi_{21}^{12}\Delta_{12}^{-} + \Pi_{22}^{12}\Delta_{22}^{-}) \quad (74)$$

and

$$\Theta_{11} = \Pi_{11}^{10}\Upsilon_{11} + \Pi_{12}^{10}\Upsilon_{21} \quad (75)$$

$$\Theta_{12} = \Pi_{11}^{10}\Upsilon_{12} + \Pi_{12}^{10}\Upsilon_{22} \quad (76)$$

$$\Theta_{21} = \Pi_{21}^{10}\Upsilon_{11} + \Pi_{22}^{10}\Upsilon_{21} \quad (77)$$

$$\Theta_{22} = \Pi_{21}^{10}\Upsilon_{12} + \Pi_{22}^{10}\Upsilon_{22} \quad (78)$$

and

$$\Sigma_{11} = (\Omega^{10}\Omega^{12}\chi^{+}\chi^{-} - \Theta_{22})(\Omega^{01} + \Pi_{11}^{01}) + \Theta_{12}\Pi_{21}^{01} \quad (79)$$

$$\Sigma_{12} = (\Omega^{10}\Omega^{12}\chi^{+}\chi^{-} - \Theta_{22})\Pi_{12}^{01} + \Theta_{12}(\Omega^{01} + \Pi_{22}^{01}) \quad (80)$$

$$\Sigma_{21} = (\Omega^{10}\Omega^{12}\chi^{+}\chi^{-} - \Theta_{11})\Pi_{21}^{01} + \Theta_{21}(\Omega^{01} + \Pi_{11}^{01}) \quad (81)$$

$$\Sigma_{22} = (\Omega^{10}\Omega^{12}\chi^{+}\chi^{-} - \Theta_{11})(\Omega^{01} + \Pi_{22}^{01}) + \Theta_{21}\Pi_{12}^{01} \quad (82)$$

and

$$Q_A = \varepsilon_g k_{t,1}^2 k_{t,2}^2(\varpi_1\xi_2 - \varpi_2\xi_1) \quad (83)$$

$$Q_B^{\pm} = \varepsilon_g \varpi_1\varpi_2(k_{t,1}^2\alpha_2^{\pm} - k_{t,2}^2\alpha_1^{\pm}) \quad (84)$$

$$Q_C^{\pm} = k_{t,1}^2\zeta_2^{\pm}\xi_1 - k_{t,2}^2\zeta_1^{\pm}\xi_2 \quad (85)$$

$$Q_D^{\pm} = \zeta_2^{\pm}\alpha_1^{\pm}\varpi_1 - \zeta_1^{\pm}\alpha_2^{\pm}\varpi_2 \quad (86)$$

$$Q_E^{\pm} = \varepsilon_g k_0^2(k_{t,1}^2\zeta_2^{\pm}\varpi_1 - k_{t,2}^2\zeta_1^{\pm}\varpi_2) \quad (87)$$

and

$$\zeta_j^{\pm} = \varepsilon_g k_x\varpi_j \pm \varepsilon_a\xi_j\gamma_{z,j} \quad (88)$$

$$\alpha_j^{\pm} = k_x\xi_j \pm \varepsilon_g k_0^2\gamma_{z,j} \quad (89)$$

$$\chi^{\pm} = k_{t,1}^2\xi_1\varpi_2\alpha_2^{\pm} - k_{t,2}^2\xi_2\varpi_1\alpha_1^{\pm} \quad (90)$$

and

$$\beta_j^{\pm} = k_x \mp i\gamma_j\delta_j,\ \phi_j^{\pm} = \delta_j k_x \mp i\gamma_j(\theta_j - 1)$$
$$\delta_j = ik_0^2\varepsilon_g/\xi_j,\ \theta_j = -k_{t,j}^2/\varpi_j,\ \gamma_0 = \sqrt{k_x^2 + k_y^2 - k_0^2\varepsilon_r}$$
$$\xi_j = k_0^2\varepsilon_t - k_{b,j}^2,\ \varpi_j = k_0^2\varepsilon_a - k_{t,j}^2$$
$$k_{t,j}^2 = k_x^2 - \gamma_j^2,\ k_{b,j}^2 = k_{t,j}^2 + k_y^2. \quad (91)$$

ACKNOWLEDGMENT

Matlab code for the Green function is available on Code Ocean, DOI 10.24433/CO.7785417.v1.

REFERENCES

[1] M. S. Kushwaha and P. Halevi, "Magnetoplasmons in thin films in the Voigt configuration," *Phys. Rev. B*, vol. 36, no. 11, pp. 5960–5967, Jul. 2002.

[2] S. R. Seshadri, "Excitation of surface waves on a perfectly conducting screen covered with anisotropic plasma," *IRE Trans. Microw. Theory Tech.*, vol. 10, no. 6, pp. 573–578, Nov. 1962.

[3] D. Bolle and S. Talisa, "Fundamental considerations in millimeter and near-millimeter component design employing magnetoplasmons," *IEEE Trans. Microw. Theory Techn.*, vol. MTT-29, no. 9, pp. 916–923, Sep. 1981.

[4] J. J. Brion, R. F. Wallis, A. Hartstein, and E. Burstein, "Theory of surface magnetoplasmons in semiconductors," *Phys. Rev. Lett.*, vol. 28, no. 22, pp. 1455–1458, May 1972.

[5] A. G. Schuchinsky and X. Yan, "Migration and collision of magnetoplasmon modes in magnetised planar semiconductor-dielectric layered structures," in *Metamaterials and Plasmonics: Fundamentals, Modelling, Applications* (NATO Science for Peace and Security Series B: Physics and Biophysics), S. Zouhdi, A. Sihvola, and A. P. Vinogradov, Eds. Dordrecht, The Netherlands: Springer, 2009.

[6] M. S. Kushwaha, "Plasmons and magnetoplasmons in semiconductor heterostructures," *Surf. Sci. Rep.*, vol. 41, nos. 1–8, pp. 1–416, Mar. 2001.

[7] A. R. Davoyan and N. Engheta, "Theory of wave propagation in magnetized near-zero-epsilon metamaterials: Evidence for one-way photonic states and magnetically switched transparency and opacity," *Phys. Rev. Lett.*, vol. 111, Dec. 2013, Art. no. 257401.

[8] T. Ozawa *et al.*, "Topological photonics," *Rev. Mod. Phys.*, vol. 91, Mar. 2019, Art. no. 015006.

[9] L. Lu, J. D. Joannopoulos, and M. Soljačić, "Topological photonics," *Nature Photon.*, vol. 8, no. 11, pp. 821–829, Nov. 2014.

[10] M. C. Rechtsman *et al.*, "Photonic Floquet topological insulators," *Nature*, vol. 496, no. 7444, pp. 196–200, Apr. 2013.

[11] Z. Wang, Y. D. Chong, J. D. Joannopoulos, and M. Soljačić, "Reflection-free one-way edge modes in a gyromagnetic photonic crystal," *Phys. Rev. Lett.*, vol. 100, Jan. 2008, Art. no. 013905.

[12] Z. Yu, G. Veronis, Z. Wang, and S. Fan, "One-way electromagnetic waveguide formed at the interface between a plasmonic metal under a static magnetic field and a photonic crystal," *Phys. Rev. Lett.*, vol. 100, Jan. 2008, Art. no. 023902.

[13] B. Yang, M. Lawrence, W.Gao, Q. Guo, and S. Zhang, "One-way helical electromagnetic wave propagation supported by magnetized plasma," *Sci. Rep.*, vol. 6, Feb. 2016, Art. no. 21461.

[14] M. G. Silveirinha, "Chern invariants for continuous media," *Phys. Rev. B, Condens. Matter*, vol. 92, no. 12, 2015. Art. no. 125153.
[15] F. D. M. Haldane and S. Raghu, "Possible realization of directional optical waveguides in photonic crystals with broken time-reversal symmetry," *Phys. Rev. Lett.*, vol. 100, no. 1, Jan. 2008, Art. no. 013904.
[16] S. Raghu and F. D. M. Haldane, "Analogs of quantum-Hall-effect edge states in photonic crystals," *Phys. Rev. A*, vol. 78, no. 3, pp. 033834-1–033834-21, Sep. 2008.
[17] S. A. H. Gangaraj, M. G. Silveirinha, and G. W. Hanson, "Berry phase, berry connection, and chern number for a continuum bianisotropic material from a classical electromagnetics perspective," *IEEE J. Multiscale Multiphys. Comput. Tech.*, vol. 2, pp. 3–17, Jan. 2017.
[18] S. A. Skirlo, L. Lu, and M. Soljačić, "Multimode one-way waveguides of large Chern numbers," *Phys. Rev. lett.*, vol. 113, Sep. 2014, Art. no. 113904.
[19] S. A. H. Gangaraj, A. Nemilentsau, and G. W. Hanson, "The effects of three-dimensional defects on one-way surface plasmon propagation for photonic topological insulators comprised of continuum media," *Sci. Rep.*, vol. 6, Jul. 2016, Art. no. 30055.
[20] S. A. H. Gangaraj, G. W. Hanson, and M. Antezza, "Robust entanglement with three-dimensional nonreciprocal photonic topological insulators," *Phys. Rev. A*, vol. 95, Jun. 2017, Art. no. 063807.
[21] M. G. Silveirinha, S. A. H. Gangaraj, G. W. Hanson, and M. Antezza, "Fluctuation-induced forces on an atom near a photonic topological material," *Phys. Rev. A*, vol. 97, Feb. 2018, Art. no. 022509.
[22] S. A. H. Gangaraj, G. W. Hanson, M. Antezza, and M. G. Silveirinha, "Spontaneous lateral atomic recoil force close to a photonic topological material," *Phys. Rev. B,* vol. 97, May 2018, Art. no. 201108.
[23] S. A. H. Gangaraj, G. W. Hanson, M. G. Silveirinha, K. Shastri, M. Antezza, and F. Monticone, "Unidirectional and diffractionless surface plasmon polaritons on three-dimensional nonreciprocal plasmonic platforms," *Phys. Rev. B,* vol. 99, Jun. 2019, Art. no. 245414.
[24] Y. Mazor and B. Z. Steinberg, "Metaweaves: Sector-way nonreciprocal metasurfaces," *Phys. Rev. Lett.*, vol. 15, Apr. 2014, Art. no. 153901.
[25] A. Leviyev *et al.*, "Nonreciprocity and one-way topological transitions in hyperbolic metamaterials," *APL Photon.*, vol. 2, no. 7, Jul. 2017, Art. no. 076103.
[26] E. D. Palik, R. Kaplan, R. W. Gammon, H. Kaplan, R. F. Wallis, and J. J. Quinn, "Coupled surface magnetoplasmon-optic-phonon polariton modes on InSb," *Phys. Rev. B,* vol. 13, no. 6, pp. 2497–2506, Jul. 2002.
[27] S. Buddhiraju *et al.*, "Absence of unidirectionally propagating surface plasmon-polaritons at nonreciprocal metal-dielectric interfaces," *Nature Commun.*, vol. 11, p. 674, 2020, doi: 10.1038/s41467-020-14504-9.
[28] S. A. Hassani Gangaraj and F. Monticone, "Do truly unidirectional surface plasmon-polaritons exist?" *Optica*, vol. 6, no. 9, p. 1158, Sep. 2019.
[29] H. C. Chen, *Theory of Electromagnetic Waves: A Coordinate-Free Approach*. New York, NY, USA: McGraw-Hill, 1983.
[30] F. I. Fedorov, "Optics of anisotropic media," in *Proc. Izd. Akad. Nauk BSSR*, Minsk, Belarus, 1958, p. 29.
[31] F. I. Fedorov, *Teoriya Girotropii* (Gyrotropy Theory). Minsk, Belarus: Naukai I Tekhnika, 1976.
[32] F. I. Fedorov, "Letter to the editor," *Radio Sci.*, vol. 26, no. 6, p. 1435, Jun. 1991.
[33] H. C. Chen, "Reply to letter to the editor," *Radio Sci.*, vol. 26, no. 6, p. 1436, Jun. 1991.
[34] W. Gao, B. Yang, M. Lawrence, F. Fang, B. Béri, and S. Zhang, "Photonic Weyl degeneracies in magnetized plasma," *Nature Commun.*, vol. 7, no. 1, 2016, Art. no. 12435.
[35] M. G. Silveirinha, "Optical instabilities and spontaneous light emission by polarizable moving matter," *Phys. Rev. X*, vol. 4, Jul. 2014, Art. no. 031013.